Journal of
Applied Crystallography
ISSN 0021-8898

Received 16 February 2006
Accepted 25 May 2006

In situ SAXS studies of the morphological changes of an alumina–zirconia–silicate ceramic during its formation

Daniel Le Messurier,[a]* Rudolf Winter[a] and Christopher M. Martin[b]

[a]Materials Physics, University of Wales, Aberystwyth, SY23 3BZ, Wales, and [b]CLRC Daresbury Laboratory, Warrington, WA4 4AD, England. Correspondence e-mail: ruw@aber.ac.uk

Small-angle X-ray scattering is used at two energies, one either side of the zirconium *K*-edge, to probe the *in situ* formation of an alumina–zirconia–silicate ceramic. The use of energies either side of the edge allows the decomposition of information regarding the scattering from the zirconia particles from that of the glass matrix. Porod slope data show how the nanoparticles progress from being relatively isolated particles to becoming agglomerates as the pore network in the glass collapses. The shape of the agglomerates resembles the pore network of the glass at low temperature. The Guinier radii of the particles show the growth of the agglomerates past the Littleton softening point, whilst still resolving the primary particles.

1. Introduction

Refractory materials are commonly used in commercial systems where resistance to high temperatures and/or chemical attack are of paramount importance. These commercial refractories are typically made of materials such as alumina, zirconia, silica and a silicate-based bonding phase to allow for the thermal expansion of the refractory. In order to study these materials in a reasonable time scale, a model system has been designed utilizing the large surface area of nano-scale particles (nanoparticles). These nanoparticles are embedded in a sodium silicate glass to form a ceramic (nanocomposite). This nanocomposite system, with its large nanoparticle to glass surface area, allows the study of different commercially interesting situations, *e.g.* corrosion, in reasonable time scales.

Small-angle X-ray scattering (SAXS) is used at multiple energies to probe the *in situ* formation of an alumina–zirconia–silicate ceramic. By choosing energies below the zirconium *K*-edge (17.98 keV) and above the edge (18.05 keV), we are able to distinguish between the zirconia particles and the surrounding glass matrix. The energies have been chosen such that the zirconium signal is attenuated in the scattering pattern obtained above the absorption edge. By having the zirconium signal reduced in one of the scattering patterns, we are able to infer the contribution from the zirconia particles and thus distinguish the scattering from the glass matrix from that of the zirconia particles. The scattering pattern obtained from a SAXS experiment can be expressed as

$$I = S(q)(I_0/A)(\Delta\Omega), \tag{1}$$

where I_0 is the primary-beam intensity produced by a beam of cross-sectional area A, $(\Delta\Omega)$ is the solid angle subtended at the sample by the detector, $S(q)$ is the scattering function characterizing the sample, with q being the magnitude of the scattering vector (Feigin & Svergun, 1987; Sinha, 1998).

We next consider our sample, which consists of a nanocomposite (which is a collection of nanoparticles) and a powdered glass matrix. These components have been pressed together to form a pellet in order to conduct the SAXS experiment. The sample could therefore be considered as a collection of particles situated in the pores of some porous medium, as the nanoparticles fill the gaps where several macroscopic glass grains touch. In this case, the $S(q)$ can be described in terms of one of two fractal models: surface fractal and mass fractal. For a surface fractal of fractal dimension D_s, the scattering function can be expressed as

$$S(q) = \frac{\pi(\Delta\rho)^2 S_2 l_2^{D_s-2}\Gamma(5-D_s)\sin[\pi(3-D_s)/2]}{(3-D_s)q^{6-D_s}} \tag{2}$$

with S_2 being the smooth surface area, measured at a length scale l_2 where the surface fractal behaviour cuts off, and Γ is the gamma function (Sinha, 1998; Mildner & Hall, 1986). The scattering function for a mass fractal of mass fractal dimension D can be expressed as

$$S(q) = NF^2(q)(\Delta\rho)^2\left\{1+\frac{1}{(qr)^D}\frac{D\Gamma(D-1)}{[1+(1/q^2\xi^2)]^{(D-1)/2}} \times \sin[(D-1)\tan^{-1}(q\xi)]\right\}, \tag{3}$$

where ξ is the fractal correlation length which represents a characteristic distance above which the mass distribution in the sample is no longer described by a fractal law (Sinha, 1998; Teixeira, 1988). N is the total number of particles, $F(q)$ is the average form factor, and $\Delta\rho$ is the scattering contrast, defined as $(\Delta\rho)^2 \propto f^*f = f_0^2 + 2f_0f' + (f')^2 + (f'')^2$. In this formalism

of the scattering contrast, f_0^2 is the normal SAXS signal, $2f_0 f'$ is the cross term, and $(f')^2 + (f'')^2$ is the resonant term. Here we will simplify the analysis of the SAXS patterns obtained by using a simple power law of the form

$$I(q) = I_0 q^{-\alpha}, \tag{4}$$

where I_0 and α are constants. The values of α can be determined from the slope of the Porod regime of a $\log I(q)$ *versus* $\log q$ plot. From these values, the mass (D) and surface (D_s) fractal dimension can be calculated. For a mass fractal, $\alpha = D$, so $1 \leq \alpha \leq 3$ since $1 \leq D \leq 3$, whereas for a surface fractal, $\alpha = 6 - D_s$, so $3 \leq \alpha \leq 4$, since $2 \leq D_s \leq 3$. One other important parameter which can be obtained from the SAXS scattering patterns is the Guinier radius, R_g. The Guinier radius is linked to the radius of gyration of the constituents which contribute to the scattering contrast by a shape-dependent prefactor, as long as the particle sizes are in the range $1/q_{max}$ to $1/q_{min}$. This is seen experimentally as a 'hump' in the scattering pattern plotted in log–log format, which can be reproduced by using an exponential function of the form:

$$I(q) = A \exp\left(R_g^2 q^2/3\right) + C, \tag{5}$$

where A and C are constants, and R_g is the Guinier radius.

2. Sample preparation

The sample used in this investigation consists of sol–gel-produced alumina–zirconia nanoparticles and a sodium silicate glass. The alumina–zirconia nanoparticles were produced by using aluminium chloride, $AlCl_3$, and zirconium tetrachloride, $ZrCl_4$, in a molar ratio of 1:9, as precursors, which were subsequently mixed with ammonium hydroxide, NH_4OH to form a gel (Winnubst *et al.*, 1989; Prabhu & Bourell, 1995). This gel was then washed and dried several times to remove the chlorine and to produce a powder. The sol–gel-prepared nanoparticles were dried at a temperature of 373 K to remove the excess water, but at a sufficiently low temperature to avoid calcination. Other nanocomposites with different Zr:Al ratios were produced and were subjected to the same experimental conditions; however they differ only in the extent to which they absorb radiation.

The sodium silicate glass was produced by mixing 0.3 mol quartz, SiO_2, with 0.1 mol sodium carbonate, Na_2CO_3. This mixture was then heated at 1573 K for 2 h, then 1623 K for 0.5 h, and finally at 1673 K for 0.5 h. This time–temperature programme was used in order to produce a homogeneous glass melt, which was then allowed to cool in air under its own thermal gradient. The resulting glass was then ball-milled briefly to produce a fine glass powder. The glass was not annealed to remove stresses as this was not considered a necessary step after ball-milling. Samples were prepared by mixing 50 wt% nanoparticles with 50 wt% glass powder and pressed into a 13 mm diameter, 400 µm thick pellet using a force of 10 tonne. The molar percentages of the constituent elements are Si 16.76%, O 60.89%, Al 1.12%, Na 11.17% and Zr 10.06%, while the volume fractions, disregarding pores as these change with temperature, are glass 71.8%, Al_2O_3 1.9% and ZrO_2 26.3%.

3. Experimental

SAXS was conducted using beamline 6.2 at the Synchrotron Radiation Source (SRS) in Daresbury, England. Beamline 6.2 uses a two-crystal Si(111) monochromator to produce X-rays in the range 5–18 keV and a one-dimensional RAPID2 small-angle detector to record SAXS patterns (Tang *et al.*, 2004). The sample pellet was mounted in a small electric furnace, which was mounted in-line such that the pre- and post-scattering X-rays were able to pass uninhibited through two mica windows. This furnace allowed heating at a rate of 15 K min^{-1} to a maximum temperature of 1273 K (Shaw *et al.*, 1999). SAXS patterns were taken at energies of 17.98 and 18.05 keV, alternately, during the same heating cycle, with the temperature increasing from 623 to 998 K at intervals of 25 K.

The choice of two energies on opposite sides of the edge instead of the standard anomalous SAXS experiment, where several energies just below the edge and one far removed from it are used, is due to the difficulty in determining the accurate position of the edge. There is a chemical shift of the edge position of approximately 8 eV between our sample and Zr foil, which changes by several eV as the experiment progresses (Fig. 1). As an accurate knowledge of the position of the edge is critical in anomalous SAXS in order to determine the exact contrast as a function of energy, we settled for the largest obtainable contrast between above and below the edge, which is smaller but not subject to the error associated with the edge shift (Winter *et al.*, 2006). This contrast can easily be seen in the scattering patterns obtained from above and below the edge (Fig. 2).

Since our sample was initially a pressed pellet, its density will change during heating due to the removal of pores, and to a lesser extent, thermal expansion. An indication of the amount of densification can be obtained by an application of

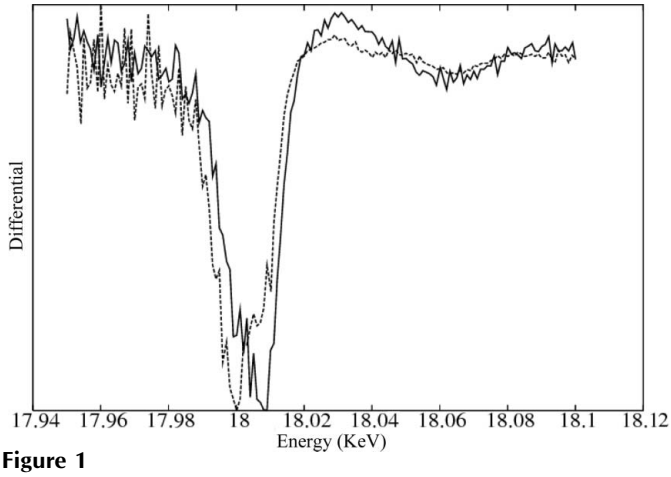

Figure 1
Scanning the energy accurately reveals the location of the edge. The solid line is the un-annealed sample, and the dotted line is the annealed sample. There is a clear chemical shift between the annealed and un-annealed samples.

Beer's law, which is an exponential law relating the transmission of the sample to the sample density and sample thickness:

$$\tau = \exp(-C\rho t), \tag{6}$$

where τ is the transmission, ρ the density, t the sample thickness and C the mass absorption coefficient of the sample. An indication of the densification of the sample can be obtained by plotting the product of density and thickness against temperature (Fig. 3), and measuring the initial and final thicknesses of the sample to see by how much the sample thickness has altered. There are two main features which are of interest in Fig. 3. From 723 to 773 K (just below the Littleton softening point) there is a plateau region in the general increase of density × thickness, indicating no significant change in physical sample dimensions. At 873 K, the maximum value of density × thickness has been achieved, and at higher temperatures the density × thickness product starts to decrease.

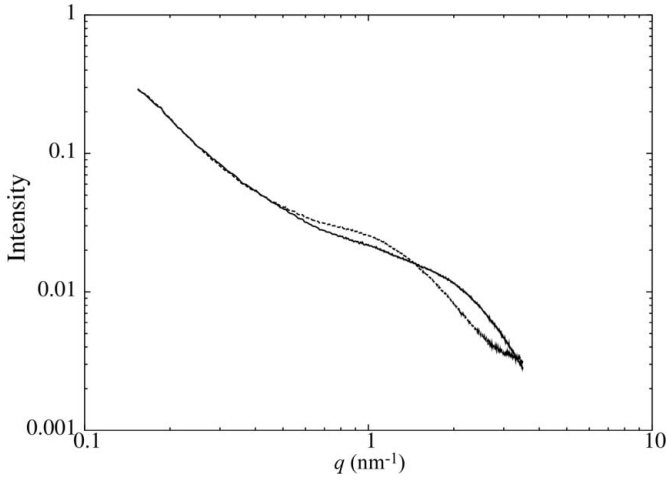

Figure 2
The scattering patterns obtained at energies of 17.98 keV (solid line) and 18.05 keV (dotted line) and a temperature of 723 K.

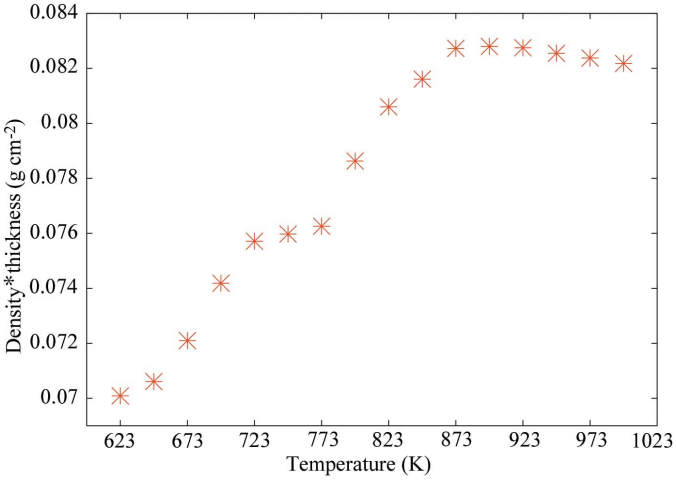

Figure 3
The variation of the product of sample density and thickness as the temperature increases during sample heating.

4. Results

The scattering patterns obtained need to be subjected to some corrections before analysis of the Porod slopes and Guinier radii can be undertaken. It is necessary to correct the background scattering patterns for the sample transmission at each temperature. Although the background was recorded at room temperature, the sample transmission changes during heating due to the densification of the sample (Fig. 3). Therefore, a transmission-corrected background signal is subtracted from the high-temperature runs at each energy. There is some fluorescence in the scattering patterns obtained at 18.05 keV arising from the 10.06 at.% of zirconium within the sample. This fluorescence has no angular dependence and has not been removed from the scattering patterns. This fluorescence contribution has been noted whilst conducting analysis of the scattering patterns, and care has been taken to ensure that the regions used for analysis have not extended into the high-q limit near the edge of the detector, where fluorescence is dominant.

The slope analysis of the Porod regime was achieved by weighted least-squares regression of equation (4) (Fig. 4B). As a consequence of the high energies used to create the scattering contrast, we have a very compressed q scale which does unfortunately give a very short Porod region. The region used for fitting is limited to the linear section and does not extend into the detector range where there would be a high fluorescence contribution. The Guinier radii were obtained by fitting a unified Guinier exponential/power law model to the scattering pattern as described by Beaucage (1996), Liu *et al.* (1999) and Hummel *et al.* (1997). The unified model, in essence, is a superposition of equations (4) and (5) and is an approximate form that describes the complex morphology of the sample over a range of structural levels. A structural level in scattering is described by Guinier's law [equation (5), Fig. 4A] and a structurally limited power law [equation (4)], which on a log–log plot is reflected by a knee and a linear region (Beaucage, 1996). Displaying the fit over the knee in the log–log plot as a traditional Guinier plot (Guinier &

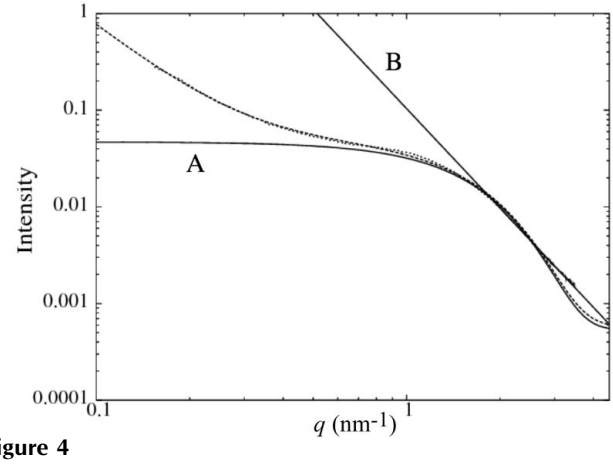

Figure 4
The scattering pattern obtained at 723 K showing the functions used for fitting the Guinier and Porod regions [dotted line: data; solid line: Guinier (A) and Porod (B) functions; dashed line: unified model fit].

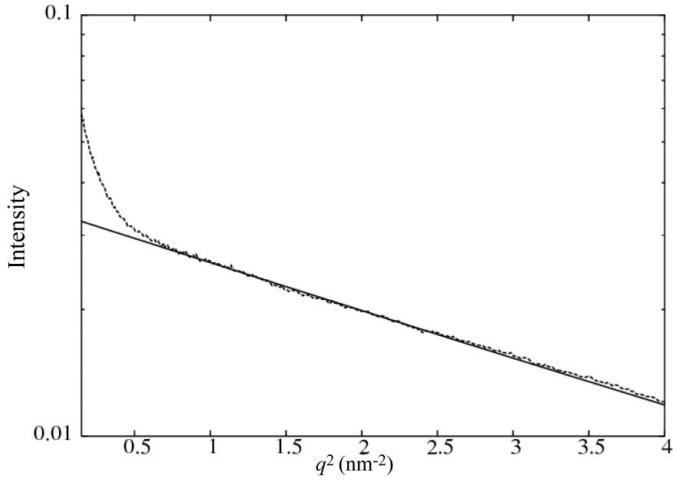

Figure 5
Guinier plot of $\log I(q)$ *versus* q^2 showing the fit of the Guinier part of the unified model (solid line) to the scattering pattern obtained at 648 K and 17.98 keV (dotted line).

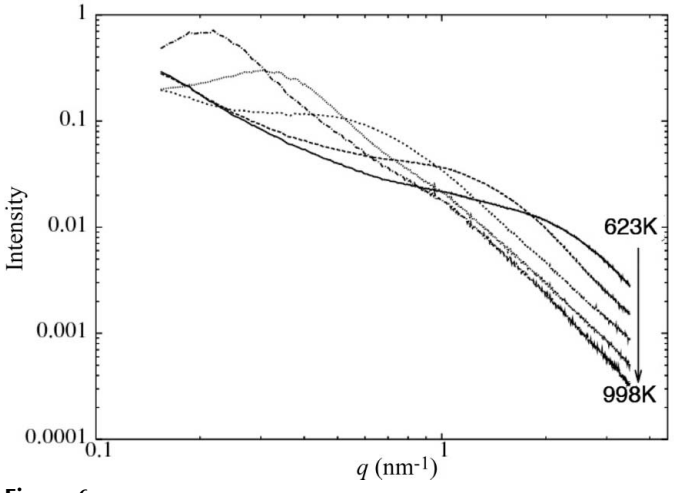

Figure 6
A stack plot of the scattering patterns obtained at an energy of 17.98 keV and temperatures of 623, 723, 823, 923, 998 K.

Fournet, 1955) of $\log I(q)$ *versus* q^2 shows the quality of the fit used (Fig. 5).

5. Discussion

At higher temperatures, the scattering patterns exhibit a clear maximum in the log–log plot of $I(q)$ *versus* q, indicating that particle–particle interactions are present [$S(q) \neq 1$] (Fig. 6). This greatly complicates the analysis as most formalisms are not strictly valid except in the dilute solution limit. With these points in mind, the values obtained from the Guinier analysis are subject to systematic errors. However, *in situ* experiments are concerned with trends on variation of a parameter, such as temperature, rather than absolute values, and clear trends emerge from this type of analysis (*cf.* Cheng & Shantz, 2005).

The alumina and zirconia produced from the sol–gel typically take the form of boehmite, AlO(OH), and hydrated zirconia, $ZrO_2.2H_2O$. As temperature is applied, there will be

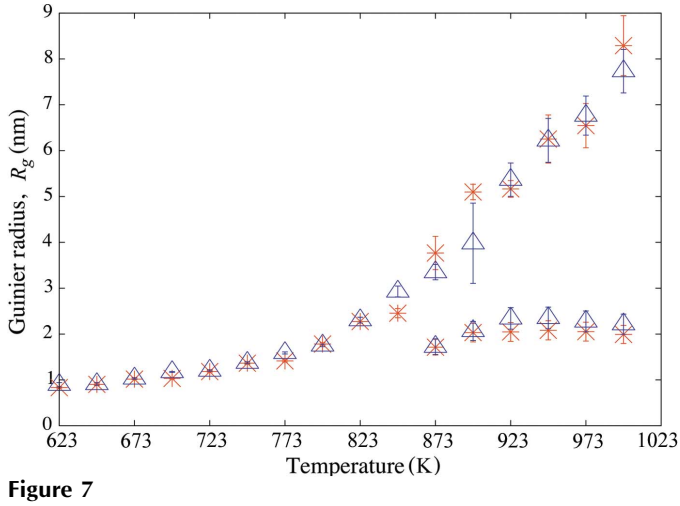

Figure 7
The results of the Guinier radius analysis clearly showing no energy dependence between the 17.98 keV experiment (stars) and the 18.05 keV experiment (triangles). One can clearly see addition of a second Guinier radius by the splitting of the single line below 873 K, into two lines above 873 K.

a release of water from the water-containing nanoparticles, initially by the zirconia/water mixture since the water is already in its molecular form, then a release of the hydroxyl groups in the boehmite. All of the water is released by the nanoparticles by 673 K.

Fig. 7 shows the Guinier radius (R_g) as a function of temperature. One can see that at low temperatures (<798 K) the values of R_g obtained at the two energies are very close to each other. Then, at a temperature between 798 and 823 K, there is a splitting of the line. This splitting indicates the appearance of a second Guinier region, *i.e.* the formation of a second hump in the scattering pattern. The point at which the values of R_g split (~813 K) is attributed to the dilatometric softening point of the glass, which is defined as the temperature at which the glass deforms under its own weight. The generally quoted associated temperature is known as the Littleton softening point, *i.e.* the temperature at which the viscosity is $10^{7.6}$ dPa s. For our glass composition, the theoretical value of the Littleton softening point is 776 K, as given by the models of Goto *et al.* (1997). The splitting of R_g is attributed to the growth of agglomerates in the sample. Past the Littleton softening point, the glass starts to soften, and the gaps between the glass grains start to change shape. Since the nanocomposite sits in these gaps, the nanoparticles start to move and form agglomerates. This also explains the constant R_g branch, as this would represent individual primary particles.

The temperature dependence of the slope of the scattering pattern (Fig. 8) is more complex and requires thought about the change in morphology of the sample as heating progresses. In the Debye model (Debye *et al.*, 1957) the treatment depends on the assumption of atomically smooth boundaries between the inhomogeneities and the host material. Also, in the limit of large scattering vectors, in the size range $\xi < q^{-1} < r_0$, where r_0 is the typical interatomic distance, the Debye model predicts the characteristic q^{-4} Porod power-law beha-

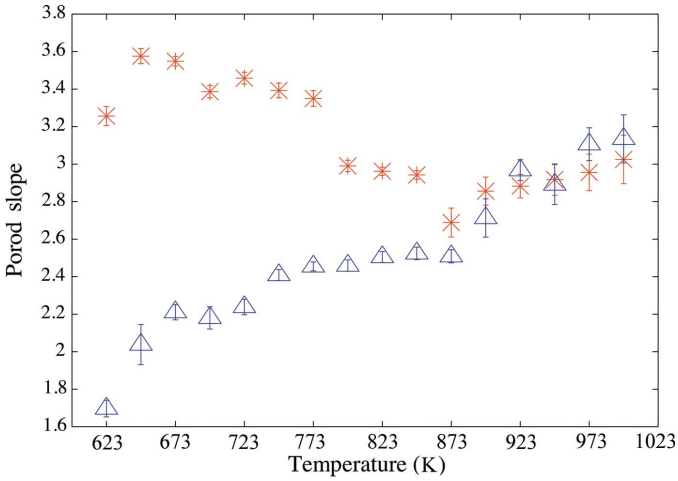

Figure 8
The results of the Porod slope analysis clearly showing an energy dependence between the 17.98 keV experiment (stars) and the 18.05 keV experiment (triangles).

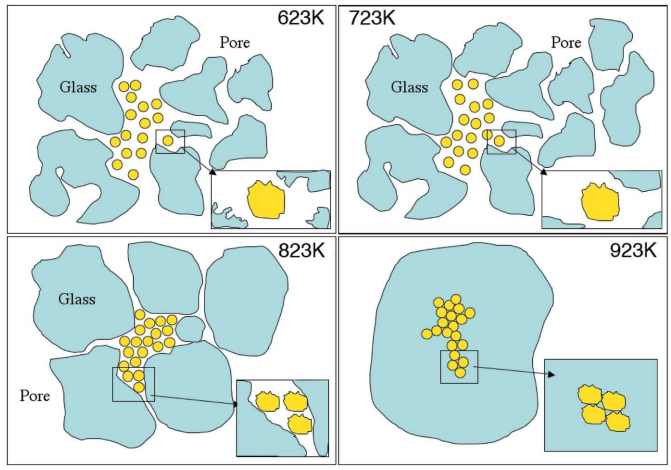

Figure 9
Schematic representation of the proposed model.

viour. Again, this requires that the interfaces are regarded as smooth on an atomic scale. In practice, we observe that none of our data obeys this law, though all have a power-law q^{-n} dependence, where n (which we call the Porod exponent) is non-integral and less than 4.

Non-integral power-law scattering in the Porod region may also be exhibited by systems in which the size distribution of the scattering inhomogeneities is itself a power law (Schmidt, 1982), with scattering proportional to q^{-n} arising from a particle (or pore) size distribution proportional to r^2. However, particles grown by condensation processes such as sol–gel and vapour deposition techniques are usually subject to a log-normal size distribution because the reaction cross section depends on the surface to volume ratio of the particles (Gleiter, 1989).

The most simplistic model which fits the data and our knowledge of the initial microstructure of the sample is that of a combination of surface and mass fractals. It is with this model in mind that we interpret our data.

The dominating contrast in the 18.05 keV data below 773 K is between glass and air, since there will be few nanoparticles in contact with the glass compared with the contact area between glass and pore (air). The geometry of this glass–pore network can be described by using a mass fractal model [equation (3)]. The 18.05 keV data sets can be regarded as containing a minimal amount of information about the zirconia nanoparticles, since the scattering arising from the glass (and the alumina nanoparticles) is largely unaffected by the change in energy. As the temperature increases, the rough surfaces of the glass grains start to smoothen as the energy required for deformation on the atomic length scale is surpassed. Above 773 K, the glass starts to soften even on a larger length scale, and the grain cores start to deform under their own weight; thus the pores reduce in size pushing the nanoparticles together into denser-packed agglomerates. This causes the dominant contrast at 18.05 keV to change and become a contrast between glass–nanoparticles–air. As the temperature rises above 873 K, the contrast changes to become solely between the glass and the nanoparticles.

The 17.98 keV data are different since they contain full information regarding the zirconia particles. Below 773 K, the dominating contrast is between the zirconia nanoparticles and air, since the nanoparticles sit in the pores of the glass powder. Above 773 K, there is a transition from being dominated by a contrast between nanoparticles and air to a contrast between nanoparticles and glass. This is due to the onset of a larger-scale deformation of the glass around the nanoparticles, thus reducing the pore size and forcing the nanoparticles to compact. Above 873 K, the glass has deformed significantly such that the nanoparticles have been fully compacted into agglomerates with no pores. The fractal nature of the agglomerates at high temperature is due to the nanoparticle agglomerates taking a shape similar to the initial pore structure. This situation differs from the original fractal nature of the pores since the fractal correlation length is different due to the fractal structure being built from small primary particles.

Fig. 9 shows a schematic representation of the proposed model. The first box (623 K) shows the initial morphology of the sample, where the nanoparticles are sitting loosely in the pores and the glass grains have a rough surface. As temperature increases (723 K box), the glass grains start to become less rough on the surface, as the energy necessary for movement on an atomic scale is surpassed. With further heating past the Littleton softening point (823 K box) there is deformation on a much larger scale, causing the pores to collapse. This causes the nanoparticles to be pushed together to form agglomerates. At high temperatures (923 K) the majority of the pores have been removed from the sample, leaving the nanoparticles in agglomerates whose shape resembles the initial pore network.

6. Conclusion

The formation of an alumina–zirconia–silicate ceramic has been investigated using *in situ* SAXS at two different energies, one above and one below the zirconium *K*-edge. It has been

shown that past the Littleton softening point of the glass, the nanoparticles start to arrange themselves to form agglomerates in the pores of the glass. By taking the Porod-regime slope, one can obtain information regarding the fractal nature of the components of the sample.

The 17.98 keV data show how the nanoparticles initially have a rough surface, and that as the temperature increases, they are forced together by the collapse of the pores to form agglomerates which resemble the shape of the initial pore network of the glass. The 18.05 keV Porod slope data show how the glass starts as a collection of jagged-shaped grains, then as heating progresses the glass grains soften and congeal to form a continuous glass matrix. By looking at the Guinier radii at 17.98 keV, one can see the growth of agglomerates past the Littleton softening point, while the primary particles can still be resolved.

The authors would like to thank Chiu Tang, then station scientist at beamline 6.2 of the SRS in Daresbury, who is now at the Diamond Light Source. Armin Hoell of the Hahn-Meitner-Institut Berlin is thanked for his assistance during the data analysis. DLM would like to thank Pilkington Plc and EPSRC for a studentship from the Collaborative Awards in Science and Engineering scheme, and CCLRC for beam time.

References

Beaucage, G. (1996). *J. Appl. Cryst.* **29**, 134–146.
Cheng, C. & Shantz, D. F. (2005). *J. Phys. Chem. B*, **109**, 13912–13920.
Debye, P., Anderson, H. R. & Brumberger, H. (1957). *J. Appl. Phys.* **28**, 679–683.
Feigin, L. A. & Svergun, D. I. (1987). *Structure Analysis by Small Angle X-ray and Neutron Scattering*, edited by G. W. Taylor. New York: Plenum.
Gleiter, H. (1989). *Prog. Mater. Sci.* **33**, 223–315.
Goto, A., Oshima, H. & Nishida, Y. (1997). *J. Volcanology Geothermal Res.* **76**, 19–327.
Guinier, A. & Fournet, G. (1955). *Small-Angle Scattering by X-rays*, pp. 126–160. London: Chapman and Hall.
Hummel, D. A., Torriani, I. L., Craievich, A. F., De la Rosa Fox, N., Ramos, A. Y. & Lyon, O. (1997). *J. Sol-Gel Sci. Technol.* **8**, 285–291.
Liu, W., Johnson, W. L., Schneider, S., Geyer, U. & Thiyagarajan, P. (1999). *Phys. Rev. B*, **59**, 11755–11759.
Mildner, D. F. R. & Hall, P. L. (1986). *J. Phys. D Appl. Phys.* **19**, 1535–1545.
Prabhu, G. B. & Bourell, D. L. (1995). *J. Nanostruct. Mater.* **6**, 361–364.
Schmidt, P. W. (1982). *J. Appl. Cryst.* **15**, 567–569.
Shaw, S., Henderson, C. M. B. & Komanschek, B. U. (1999). *Chem. Geol.* **167**, 141–159.
Sinha, S. K. (1998). *Proceedings of the Sixth Summer School on Neutron Scattering*, pp. 251–281. Singapore: World Scientific.
Tang, C. C., Martin, C. M., Laundy, D., Thompson, S. P., Diakun, G. P. & Cernik, R. J. (2004). *Nucl. Instrum. Methods Phys. Res. B*, **222**, 659–666.
Teixeira, J. (1988). *J. Appl. Cryst.* **21**, 781–785.
Winnubst, A. J. A., Grootzevert, W. F. M., Theunuissen, G. S. H. M. & Burggraaf, A. F. (1989). *J. Mater. Sci. Eng. A*, **109**, 215–219.
Winter, R., Le Messurier, D. & Martin, C. M. (2006). *Crystallogr. Rev.* Accepted.